

Zero-Threshold Rectification Using Low Energy Barrier Nano-Magnets

Shehrin Sayed,^{1,2,*} Kerem Y. Camsari,¹ Rafatul Faria,¹ and Supriyo Datta^{1,†}

¹*Electrical and Computer Engineering, Purdue University, West Lafayette, IN 47907, USA*

²*Electrical Engineering and Computer Science, University of California, Berkeley, CA 94720, USA*

(Dated: January 2, 2024)

Nanomagnets with high energy barriers (~ 40 - $60 k_B T$) have been the center of focus for various spintronics applications. Recently, low energy barrier magnets have attracted growing interest in the community for novel applications such as random number generation, stochastic oscillators, and probabilistic computation. In this paper, we predict that a low barrier magnet (LBM), either with an in-plane or perpendicular anisotropy, should exhibit zero-threshold rectification when combined with the physics of spin-momentum locking (SML) observed in high spin-orbit materials e.g. transition metals, semimetals, topological insulators, narrow band-gap semiconductors, etc. The basic idea is to measure the charge current induced spin accumulation in the SML channel using the LBM, while the magnetization of the LBM on average follows the accumulated spins due to the spin-orbit torque. Using experimentally benchmarked models, we show that these experiments can be used to characterize such stochastic magnets and extract parameters that determine (i) the spin-orbit torque induced magnetization pinning and (ii) the frequency band of rectification. We argue that the frequency band can be explained from the angular momentum conservation principles and provide an empirical expression that is valid for LBMs with in-plane and perpendicular anisotropies. The proposed structure could find application as highly sensitive passive RF detectors and as energy harvesters from weak ambient sources where standard technologies may not operate.

Nanomagnets with high energy barriers $\Delta_B \approx 40 \sim 60 k_B T$ (k_B : Boltzmann constant and T : temperature) have been the center of attention in magnetic memory industries [1, 2], since they ensure a long retention time $\tau \propto \exp(\Delta_B/k_B T)$ of the magnetic state. Recently, low energy barrier magnets (LBM) with low τ have attracted interest as random number generators (RNG) [3, 4], stochastic magnetic oscillators [5], and building blocks for probabilistic computing [6, 7].

In this paper, we predict that the well-established spin-potentiometric measurements, commonly carried out with a stable magnetic contact on top of a material with spin-momentum locking (SML) (see, for example, [8–12]) will exhibit a zero-threshold rectification of the input current when the stable magnet is replaced with an LBM. Using experimentally benchmarked models [13–15], we provide a detailed analysis of such rectification considering LBMs with both in-plane (IMA) and perpendicular (PMA) magnetic anisotropy. Specifically, we show that these experiments can be used to extract parameters of LBM that determine (i) the spin-orbit torque (SOT) induced magnetization pinning and (ii) the frequency band of the rectification. We argue that the frequency band can be explained with angular momentum conservation principles and provide an empirical expression that applies to LBMs with both IMA and PMA. We further discuss the possibility of wide band AC to DC conversion even from weak sources, which could find applications as highly sensitive passive rf detectors and as energy harvesters from ambient sources.

Spin-potentiometric measurements [13, 16–18] are commonly carried out by injecting a charge current i_c through a material with SML along \hat{x} -direction and the induced z -polarized spin voltage is measured with a stable ferromagnetic (FM) contact. The FM voltage with respect to a reference normal metal (NM) contact at the same position as FM along \hat{x} -direction (see Fig. 1(a)) is given by [18]

$$V_{fm} = m_z \frac{\alpha \xi p_0 p_f R_B}{2} i_c, \quad (1)$$

where $m_z = \pm 1$ is the z -component of the magnetization, p_f is the FM polarization, ξ is the current shunting factor [17] of the contact, p_0 is the degree of SML in the channel [13], $\alpha \approx 2/\pi$ is an angular averaging factor [13], and $R_B = (h/q^2)(1/M_t)$ is the ballistic resistance of the channel with total number of modes M_t (q : electron charge, h : Planck's constant). Eq. (1) is valid from ballistic to diffusive regime of operation [16–18].

The phenomenon described by Eq. (1) has been observed on diverse classes of materials e.g. topological insulator (TI) [8–10], Kondo insulators [19], transition metals [11], semimetals [20], and semiconductors [12]. p_0 for different materials can be somewhere in between 0 and 1 where $p_0 = 0$ represents a NM channel and $p_0 = 1$ represents a perfect TI. For Bi_2Se_3 and Pt, p_0 are ~ 0.6 and ~ 0.05 as estimated in Ref. [18] based on the experiments in Ref. [10] and Ref. [11], respectively. For a given structure, ξ can vary somewhere in between 0 and 1 where these extreme limits indicate very high and very low current shunting in the FM respectively [17, 18]. To enhance ξ , usually a thin tunnel barrier is inserted at the interface between a highly resistive SML channel (e.g. TI [8–10], semiconductor [12], etc.) and a metallic FM.

* ssayed@berkeley.edu

† datta@purdue.edu

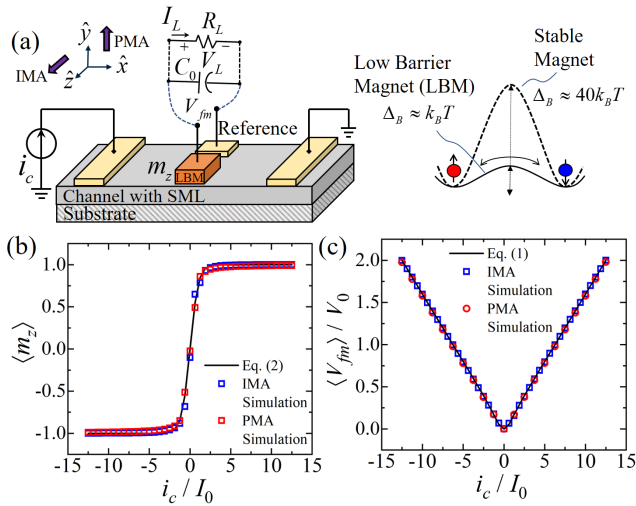


FIG. 1. **Concept of rectification.** (a) Multi-terminal rectifier structure with a low barrier magnet (LBM) on top of a channel with spin-momentum locking (SML). (b) Average magnetization ($\langle m_z \rangle$) of the LBM and (c) average voltage ($\langle V_{fm} \rangle$) between the LBM and a reference contact as a function of the input current i_c . Simulations with magnets having both in-plane and perpendicular anisotropies (IMA and PMA) are compared with Eqs. (1) and (2). I_0 for IMA and PMA are $80 \mu\text{A}$ and $1.6 \mu\text{A}$ respectively. Here, $V_0 = I_0 R_B$.

However, the tunnel barrier also degrades the spin injection into the FM from the SML channel. Such shunting effect is less severe for metallic channels (e.g. Pt, Ta, W, etc.) and a voltage described by Eq. (1) has been measured without any tunnel barrier [11]. These metallic spin-potentiometric structures have been discussed for magnetic memory applications [18] with Eq. (1) as a new read-out mechanism without conventional magnetoresistive devices.

The voltage in Eq. (1) gives same polarity irrespective of the direction of i_c , if the stable magnet in the metallic spin-potentiometric structure is replaced with an LBM with low Δ_B . For a mono-domain magnet, $\Delta_B = \frac{1}{2} H_k M_s \Omega$ [21] is determined by the anisotropy field H_k , saturation magnetization M_s , and volume Ω . Experimentally, LBM has been achieved by lowering the total moment ($M_s \Omega$) [4] or by lowering the anisotropy field (H_k) either by increasing the thickness of a PMA [22], or by making a circular IMA with no shape anisotropy [14].

The z -component of the magnetization of an LBM is random within the range $(+1, -1)$ driven by thermal noise and time-average $\langle m_z \rangle \approx 0$. Non-zero i_c in the SML channel induces z -polarized spins which applies SOT on the LBM. Thus time-average of m_z follows i_c given by the following approximate expression

$$\langle m_z \rangle \approx \tanh\left(\frac{i_c}{I_0}\right), \quad (2)$$

where I_0 is a parameter that determines the SOT induced

magnetization pinning of the LBM, which is much larger for an IMA as compared to a PMA due to the demagnetization field. Note that the i_c induced z -polarized spins in the SML channel causes a pinning of the magnetization along \hat{z} -direction which is the easy axis for IMA and hard axis for PMA (PMA easy-axis is \hat{y} -direction) in the present discussion.

We have assumed a tanh dependence in Eq. (2) for simplicity. However, the dependence of $\langle m_z \rangle$ on i_c can be described with other saturating odd-functions such as the Langevin function (see Appendix D). Eq. (2) is reasonably in agreement with detailed simulations for both IMA and PMA within the parameter space used for the present discussions (see Fig. 1(b)). We have simulated the structure in Fig. 1(a) in our SPICE compatible framework [15, 23], using our experimentally benchmarked transmission line model for SML materials [13] and stochastic Landau-Lifshitz-Gilbert (s-LLG) model for LBM [6]. The details of the simulation are given in Appendix A. Results for current, voltage, power, and frequency are normalized by I_0 , $V_0 = I_0 R_B$, $P_0 = I_0^2 R_B$, and $f_0 = I_0/q$, respectively. In all simulations, $M_t = 100$ which yields $R_B = 259 \Omega$.

For smaller input currents ($|i_c| \ll I_0$), $\tanh(i_c/I_0) \approx i_c/I_0$ and for larger input currents ($|i_c| \gg I_0$), $\tanh(i_c/I_0) \approx +1$ or -1 for $i_c > 0$ or $i_c < 0$ respectively. The time-average voltage in Eq. (1) is given by

$$\begin{aligned} \langle V_{fm} \rangle &= \frac{\alpha \xi p_0 p_f R_B}{2 I_0} i_c^2, \quad \text{for } |i_c| \ll I_0, \\ &= \frac{\alpha \xi p_0 p_f R_B}{2} |i_c|, \quad \text{for } |i_c| \gg I_0. \end{aligned}$$

Thus for any value and direction of i_c , $\langle V_{fm} \rangle$ is always of the same sign leading to a rectified voltage. The normalized simulation results for both IMA and PMA agree well with this conclusion obtained from the simple models in Eqs. (1) and (3), as shown in Fig. 1(c).

A diode like effect in TI has been theoretically discussed in the past [24] using two stable FM contacts. However, such an effect should not exist in linear response regime due to the restrictions from Onsager reciprocity [17, 25]. The discussions presented here on the multi-terminal structure with SML materials are valid in linear response. The non-linear rectification occurs due to the coupling of SML with the LBM.

$\langle V_{fm} \rangle$ corresponds to the steady-state DC voltage at the capacitor C_0 across the LBM and reference NM (see Fig. 1(a)) under no load conditions ($R_L \rightarrow \infty$). We next simulate the structure with an AC input current $i_c = i_{c0} \sin(2\pi ft)$ with amplitude i_{c0} and frequency $f = 1/T$ (see Fig. 2(a)) and observe the voltage V_L across the capacitor C_0 under the open circuit condition ($R_L \rightarrow \infty$). Simulation results of charging of C_0 are shown in Fig. 2(b) which reaches a steady-state value for $t \rightarrow \infty$. The

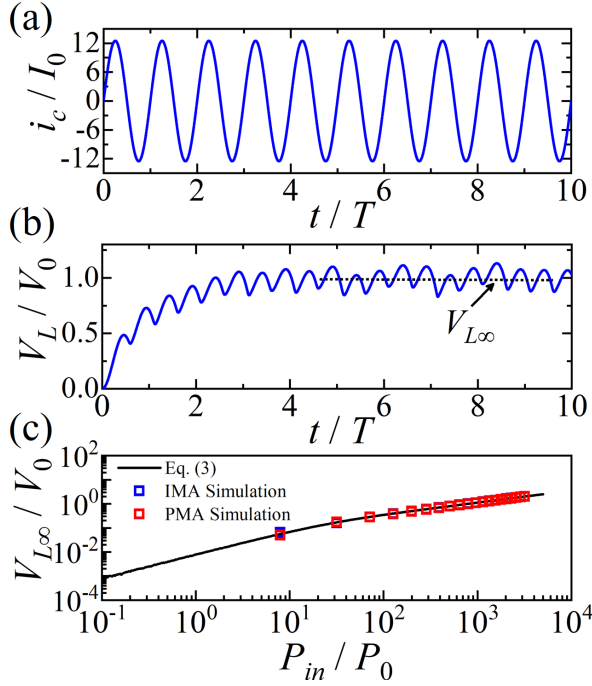


FIG. 2. **Low frequency ac to dc conversion.** (a) Input ac current i_c with period T as a function of time t . (b) Voltage across capacitor C_0 when $R_L \rightarrow \infty$ as a function of t . (c) Steady-state ($t \rightarrow \infty$) voltage $V_{L\infty}$ when $R_L \rightarrow \infty$ as a function of input ac power P_{in} . Here, $V_0 = I_0 R_B$ and $P_0 = I_0^2 R_B$.

steady-state voltage under $R_L \rightarrow \infty$ is given by

$$V_{L\infty} = \frac{1}{T} \int_0^T V_{fm} dt = \frac{\alpha \xi p_0 p_f}{2G_B} \tilde{i}_c, \quad (3)$$

where V_{fm} is given by Eq. (1), $\tilde{i}_c = \frac{2}{\pi} i_{c0}$ when $i_{c0} \gg I_0$ and $\tilde{i}_c = (i_{c0}/\sqrt{2})^2 / I_0$ when $i_{c0} \ll I_0$ (see Appendix B for details). The ripples in V_L is similar to those observed in conventional rectifiers and gets attenuated for increased C_0 .

$V_{L\infty}$ as a function of the average input AC power $P_{in} = \frac{1}{T} \int_0^T i_c^2 R_{ch} dt = \frac{1}{2} i_{c0}^2 R_{ch}$ (R_{ch} : channel resistance) is shown in Fig. 2(c) and compared with both IMA and PMA simulations. From Eq. (3), we see that $V_{L\infty}$ scales $\propto \sqrt{P_{in}}$ when $i_{c0} \gg I_0$ and scales $\propto P_{in}$ when $i_{c0} \ll I_0$. Thus the slope in Fig. 2(c) degrades inversely proportional to $\sqrt{P_{in}}$ for $i_{c0} \gg I_0$ and becomes maximum for $i_{c0} \ll I_0$, given by

$$\left(\frac{dV_{L\infty}}{dP_{in}} \right)_{\max} = \frac{\alpha \xi p_0 p_f}{2} \frac{R_B}{I_0 R_{ch}}. \quad (4)$$

See Appendix C for derivation.

The slope of $V_{L\infty}$ vs. P_{in} is often provides the sensitivity of a diode for RF detection applications [26–29]. Recently, magnetic tunnel junction (MTJ) diodes with stable magnet as free layer and under an external

dc current bias have demonstrated orders of magnitude higher sensitivity compared to the state-of-the-art Schottky diodes [27, 28]. However, the reported no-bias sensitivity is lower or comparable to that of semiconductor diodes. Eq. (4) indicates that the no-bias sensitivity of the metallic structure in Fig. 1(a) can be high if I_0 is very low. I_0 depends on the geometry and material parameters. For a given structure, I_0 can be determined experimentally by using characteristics curves similar to those in Figs. 1(b) and/or (c).

To understand the order of magnitude of I_0 in a given structure, we derive a simple expression starting from the steady-state probability distribution solution of the Fokker-Planck Equation [30] by considering easy-axis pinning of PMA magnet (see Appendix D for the derivation), given by

$$I_0 \approx \frac{6q}{\hbar} \frac{k_B T \alpha_g}{\beta}, \quad (5)$$

where α_g is the Gilbert damping and β is the charge to spin current conversion ratio. Eq. (5) is reasonably valid up to $\Delta_B \approx k_B T$ and provides correct order of magnitude up to several $k_B T$ which has been discussed in the Appendix D. With $\alpha_g = 0.01$ and $T = 300$ K we have $I_0 \approx 0.37 \mu\text{A}/\beta$. For a Py LBM of dimension of $49 \text{ nm} \times 61 \text{ nm} \times 5 \text{ nm}$ like the one used in Ref. [22] and 2 nm thick Pt channel, β can be ~ 2 as estimated from the charge to spin conversion ratio reported in Ref. [31]. Note that β can be much higher based on the geometry and the choice of the SML material.

For Bi_2Se_3 and Pt, we roughly estimate the sensitivity as 21,000 and 860 mV/mW respectively, assuming 2D SML channel of width $w = 210 \text{ nm}$ and length $L = 500 \text{ nm}$ and a Py LBM (with $p_f \approx 0.5$ [12]). These estimations were done based on Eq. (4) using: (i) $R_B = 259 \Omega$ (Bi_2Se_3) and 58Ω (Pt), (ii) $R_{ch} \approx 6.5 \text{ k}\Omega$ (Bi_2Se_3) and $\sim 3 \text{ k}\Omega$ (Pt), (iii) $p_0 \approx 0.6$ (Bi_2Se_3) and 0.05 (Pt) [18], and (iv) $I_0 \approx 0.18 \mu\text{A}$. We have assumed $\xi \approx 1$ and the quoted estimations will be lower for higher shunting. R_B has been estimated using $M_t = k_F w / \pi$, where $k_F = 1.5 \text{ nm}^{-1}$ (Bi_2Se_3) and 6.7 nm^{-1} (Pt) [18]. The channel resistance has been estimated using $R_{ch} = R_B(L + \lambda) / \lambda$ with mean free path λ of 20 nm (Bi_2Se_3 [32]) and 10 nm (Pt [33]), respectively.

To understand the frequency limitations of the rectification, we have observed the steady-state open circuit dc voltage $V_{L\infty}$ as a function of input ac current frequency f (see Fig. 3(a)) while keeping other parameters constant. The frequency response of the proposed device is similar to a low-pass filter and the cut-off frequency f_c is given by

$$2\pi f_c = \frac{i_{s0}}{2qN_s}, \quad (6)$$

where the injected spin current amplitude $i_{s0} = \beta i_{c0}$,

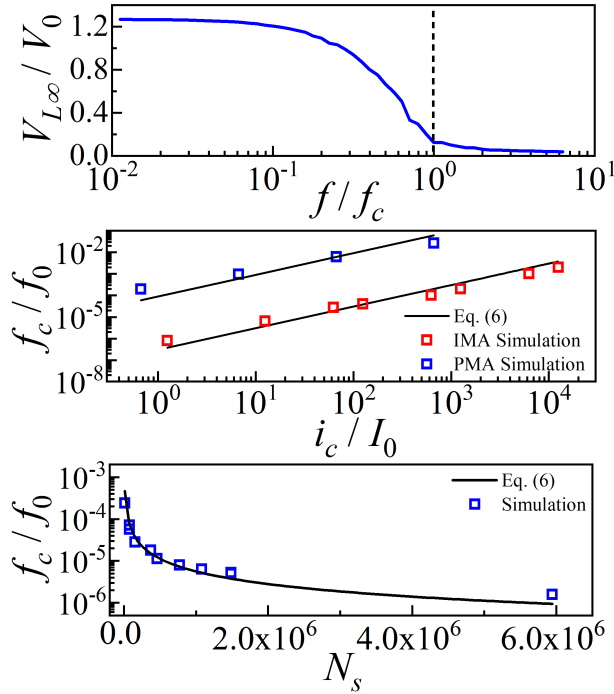


FIG. 3. **Bandwidth of operation.** (a) Frequency response of the proposed rectifier. $V_{L\infty}$ degrades rapidly by orders of magnitude near the cut-off frequency f_c . f_x is (b) proportional to i_{c0} and (c) inversely proportional to N_s , for both PMA and IMA. N_s for PMA and IMA are 10^4 and 10^6 respectively in the simulation of Fig. 3(b). Simulations are compared with Eq. (6) and shows good agreement. Here, $f_0 = I_0/q$.

$N_s = M_s\Omega/\mu_B$ is the total number of spins in the magnet and μ_B is the Bohr magneton.

Eq. (6) is an empirical expression obtained from the s-LLG simulations for a broad range of parameter values. For a given set of parameters, we have extracted f_c from a plot similar to Fig. 3(a), by taking f_c as the frequency at which $V_{L\infty}$ degrades by an order of magnitude as compared to its low frequency value. The functional dependence of f_c on i_{s0} and N_s is very similar to the functional dependence of the switching delay for stable magnets on the switching spin current and N_s [34] that arises from the principles of angular momentum conservation.

Eq. (6) shows good agreement with the SPICE simulation results for LBMs having IMA with easy-axis pinning and PMA with hard-axis pinning (see Figs. 3(b)-(c)). Fig. 3(b) shows that f_c scales linearly with i_{c0} and the conclusion seems valid even if i_{c0} changes by orders of magnitude. Fig. 3(c) shows that f_c scales inversely proportional to the N_s . The $m_z(t)$ of the LBM can follow $i_c(t)$ when $f < f_c$ but struggles to follow $i_c(t)$ when $f > f_c$. This scenario is discussed in the Appendix E with detailed simulations. A similar scenario has been observed experimentally [5] for a stochastic os-

illator made with MTJ having lower energy barrier free magnetic layer.

The no-bias high RF detection sensitivity of the proposed device indicates the possibility of energy harvesting from ambient weak RF sources and could be of interest to applications like self-powered devices and sensors [35]. The DC power delivered to the load $P_L = V_L I_L$ is maximum when load R_L is equal to the equivalent resistance R_{eq} between the LBM and the reference NM. Thus the maximum DC power transferred to the load is given by

$$P_{L,\max} = \frac{V_{L\infty}^2}{4R_{eq}}.$$

The efficiency of such RF to DC power conversion can be calculated as $\eta = P_{L,\max}/P_{in}$ and the maximum efficiency is observed for $i_{c0} \gg I_0$, which is given by

$$\eta_{\max} = \left(\frac{\xi p_0 p_f}{2\pi} \right)^2 \frac{R_B}{R_{eq}} \frac{R_B}{R_{ch}}. \quad (7)$$

The derivation is given in the Appendix F. Assuming $R_{eq} = 10R_B$ for enhanced ξ , we estimate the maximum efficiency to be 0.001% for Bi_2Se_3 and $3 \times 10^{-6}\%$ for Pt even with P_{in} in the \sim pW range with $I_0 \leq 0.37\mu\text{A}$. MTJ diodes with similar efficiency recently demonstrated the possibility of ambient RF energy harvesting to enable self-powered devices [29], however, the input power was in the μW range. Such MTJs may also be able to achieve reasonable efficiency at lower input power if the stable free layer is replaced with a LBM. However, an MTJ with tunnel barrier could be subject to high loss and power consumption compared to the metallic structure proposed here.

In conclusion, we predict the possibility of zero-threshold rectification in a multi-terminal all-metallic structure that comprises a material with spin-momentum locking and a low energy barrier magnet (LBM) with either in-plane or perpendicular anisotropy. The rectified signal can be used to characterize the LBMs and extract parameters that determine the spin-orbit torque induced magnetization pinning and the frequency band governed by angular momentum conservation principles. We further discuss the possibility of wide band AC to DC conversion even from weak sources, which could find applications as highly sensitive passive rf detectors and as energy harvesters from ambient sources.

This work was supported by ASCENT, one of six centers in JUMP, a SRC program sponsored by DARPA.

Appendix A: Simulation Setup

This section provides the details of the simulation setup in SPICE that was used to analyze the proposed rectifier.

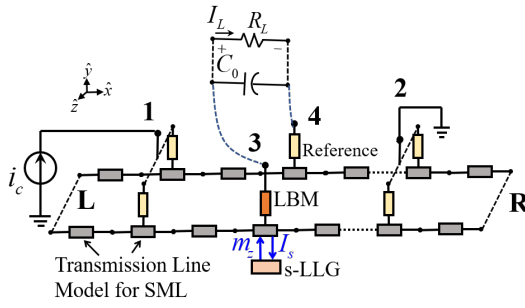


FIG. 4. SPICE simulation setup for the structure shown in Fig. 1(a) in the main manuscript. SML channel is modeled by connecting SPICE compatible transmission line model [13] in a distributed manner. The LBM is modeled with stochastic Landau-Lifshitz-Gilbert (s-LLG) SPICE model [6].

We have discretized the structure in Fig. 1(a) into 100 small sections and represented each of the small sections with the corresponding circuit model. Note that each of the nodes in Fig. 4 are two component: charge (c) and z -component of spin (s). We have connected the charge and spin terminals of the models for all the small sections in a modular fashion using standard circuit rules as shown in Fig. 4. The models are connected in a series to reconstruct the structure along length direction. We have two of such parallel chains to take into account the structure along width direction and the two chains represent the area under the LBM and the reference NM respectively. The SML block with LBM is connected to a s-LLG block which takes the spin current from the SML block as input and self-consistently solves for m_z and feeds back to the SML block.

The contacts (1, 2, 3, and 4) in this discussion are point contacts. The polarization of contacts 1, 2, and 4 are $p_f = 0$ since they represent normal metals. Polarization of contact 3 is 0.8 which represents an LBM. We set the total number of modes $M + N$ in the channel to be 100. We have assumed that the reflection with spin-flip scattering mechanism is dominant in the channel i.e. $r_{s1,2} \gg r, t_s$. The scattering rate per unit mode was set to 0.04 per lattice point.

We apply the charge open and spin ground boundary condition at the two boundaries given by

$$\begin{Bmatrix} i_c \\ v_s \end{Bmatrix}_L = \begin{Bmatrix} 0 \\ 0 \end{Bmatrix}, \quad \text{and} \quad \begin{Bmatrix} i_c \\ v_s \end{Bmatrix}_R = \begin{Bmatrix} 0 \\ 0 \end{Bmatrix}. \quad (\text{A1})$$

Here, i_c and v_s indicates boundary charge current and boundary spin voltage. Indices L and R indicate left and right boundaries respectively.

Both charge and spin terminals of contact 1 and 2 and the two boundaries of the two parallel model chains are connected together. We apply a current i_c at the charge terminal of contact 1 and make the spin terminal grounded to take into account the spin relaxation process

in the contact. We ground both charge and spin terminals of contact 2. The boundary conditions of contacts 1 and 2 are given by

$$\begin{Bmatrix} i_c \\ v_s \end{Bmatrix}_1 = \begin{Bmatrix} i_c \\ 0 \end{Bmatrix}, \quad \text{and} \quad \begin{Bmatrix} v_c \\ v_s \end{Bmatrix}_2 = \begin{Bmatrix} 0 \\ 0 \end{Bmatrix}. \quad (\text{A2})$$

We place a capacitor C_0 and load R_L across the charge terminals of contacts 3 and 4. The spin terminals of contacts 3 and 4 are grounded. The boundary conditions of the contacts 3 and 4 are given by

$$\begin{Bmatrix} i_c \\ v_s \end{Bmatrix}_3 = \begin{Bmatrix} 0 \\ 0 \end{Bmatrix}, \quad \text{and} \quad \begin{Bmatrix} i_c \\ v_s \end{Bmatrix}_4 = \begin{Bmatrix} 0 \\ 0 \end{Bmatrix}. \quad (\text{A3})$$

Appendix B: Average Output DC Voltage

This section discusses the detailed derivation of Eq. (3).

We start from Eq. (1) of the main manuscript which has been previously discussed in Ref. [18]

$$V_{fm}(t) = m_z(t) \frac{\alpha \xi p_0 p_f}{2G_B} i_c(t), \quad (\text{B1})$$

where $m_z(t)$ is given by Eq. (2). The average is calculated as

$$\begin{aligned} \langle V_{fm} \rangle &= \frac{1}{T} \int_0^T V_{fm} dt \\ &= \frac{1}{T} \frac{\alpha \xi p_0 p_f}{2G_B} \int_0^T \tanh\left(\frac{i_c(t)}{I_0}\right) i_c(t) dt. \end{aligned} \quad (\text{B2})$$

Note that the timed average of the random part in Eq. (2) is zero.

We apply $i_c = i_{c0} \sin(2\pi t/T)$. For $i_{c0} \gg I_0$, we get $\tanh(i_c(t)/I_0) \approx +1$ when $i_c(t) > 0$ and $\tanh(i_c(t)/I_0) \approx -1$ when $i_c(t) < 0$. Thus we have

$$\tanh\left(\frac{i_c(t)}{I_0}\right) \times i_c(t) \approx |i_c(t)|,$$

and from Eq. (B2), we get

$$\begin{aligned} \langle V_{fm} \rangle &= \frac{1}{T} \frac{\alpha \xi p_0 p_f}{2G_B} \int_0^T |i_c(t)| dt \\ &= \frac{1}{T} \frac{\alpha \xi p_0 p_f}{2G_B} i_{c0} \int_0^T \left| \sin\left(\frac{2\pi t}{T}\right) \right| dt \\ &= \frac{1}{T} \frac{\alpha \xi p_0 p_f}{2G_B} i_{c0} \int_0^{\frac{T}{2}} \sin\left(\frac{2\pi t}{T}\right) dt \\ &\quad + \frac{1}{T} \frac{\alpha \xi p_0 p_f}{2G_B} i_{c0} \int_{\frac{T}{2}}^T -\sin\left(\frac{2\pi t}{T}\right) dt \\ &= \frac{\alpha \xi p_0 p_f}{2G_B} \times \frac{2}{\pi} i_{c0}. \end{aligned} \quad (\text{B3})$$

For $i_{c0} \ll I_0$, we get $\tanh(i_c(t)/I_0) \approx i_c(t)/I_0$. Thus from Eq. (B2), we get

$$\begin{aligned} \langle V_{fm} \rangle &= \frac{1}{T} \frac{\alpha \xi p_0 p_f}{2G_B I_0} \int_0^T i_c^2(t) dt \\ &= \frac{1}{T} \frac{\alpha \xi p_0 p_f}{2G_B} \frac{i_{c0}^2}{I_0} \int_0^T \sin^2\left(\frac{2\pi t}{T}\right) dt \quad (\text{B4}) \\ &= \frac{\alpha \xi p_0 p_f}{2G_B} \times \frac{(i_{c0}/\sqrt{2})^2}{I_0}. \end{aligned}$$

Note that $\langle V_{fm} \rangle$ is the $V_{L\infty}$ in Eq. (3) in the main manuscript which corresponds to V_L at $R_L \rightarrow \infty$.

Appendix C: Average Output DC Voltage vs. Average Input AC Power and Sensitivity

This section discusses the dependency of average dc output voltage on average input ac power and derives the sensitivity expression in Eq. (4).

With $i_c = i_{c0} \sin(2\pi t/T)$, the average ac input power applied to the channel with resistance R_{ch} is given by

$$\begin{aligned} P_{in} &= \frac{1}{T} \int_0^T i_c^2 R_{ch} dt \\ &= \frac{i_{c0}^2 R_{ch}}{T} \int_0^T \sin^2\left(\frac{2\pi t}{T}\right) dt \quad (\text{C1}) \\ &= \left(\frac{i_{c0}}{\sqrt{2}}\right)^2 R_{ch}. \end{aligned}$$

1. Case I: $i_{c0} \gg I_0$

For $i_{c0} \gg I_0$, we have from Eq. (B3)

$$\langle V_{fm} \rangle = \frac{\alpha \xi p_0 p_f}{\pi G_B} \times \frac{\sqrt{2}}{\sqrt{R_{ch}}} \times \sqrt{P_{in}}, \quad (\text{C2})$$

and the sensitivity is given by

$$\frac{d\langle V_{fm} \rangle}{dP_{in}} = \frac{\alpha \xi p_0 p_f}{\pi G_B} \times \frac{1}{\sqrt{2R_{ch}}} \times \frac{1}{\sqrt{P_{in}}}. \quad (\text{C3})$$

The sensitivity for $i_{c0} \gg I_0$ decreases inversely proportional to $\sqrt{P_{in}}$. Sensitivity increases for decreasing P_{in} and eventually saturates to a maximum value for $i_{c0} \ll I_0$.

2. Case II: $i_{c0} \ll I_0$

For $i_{c0} \ll I_0$, we have from Eq. (B4)

$$\langle V_{fm} \rangle = \frac{\alpha \xi p_0 p_f}{2G_B R_{ch} I_0} P_{in}, \quad (\text{C4})$$

and the sensitivity is given as

$$\frac{d\langle V_{fm} \rangle}{dP_{in}} = \frac{\alpha \xi p_0 p_f}{2G_B R_{ch} I_0}, \quad (\text{C5})$$

which is shown in Eq. (4) as the maximum sensitivity.

Appendix D: Average Magnetization and Pinning Current

This section discusses the pinning current of a LBM and derives Eq. (5) starting from the steady-state solution of the Fokker-Planck Equation.

We start from the steady-state solution of probability distribution from Fokker-Planck Equation assuming a magnet with perpendicular magnetic anisotropy (PMA) (see Eq. (4.3) in Ref. [30]), given by

$$\rho(m_z) = \frac{1}{Z} \exp\left(\frac{\Delta_B}{k_B T} m_z^2 + \frac{2\Delta_B}{k_B T} \left(\frac{H_{ext}}{H_k} + \frac{i_s}{I_{s0}}\right) m_z\right), \quad (\text{D1})$$

where Z is a normalizing factor, m_z is the magnetization along easy-axis (z -axis in the present discussion), $\Delta_B = H_k M_s \Omega / 2$ is the energy barrier of a magnet with anisotropy field H_k , saturation magnetization M_s , and volume Ω , k_B is the Boltzmann constant, T is the temperature, H_{ext} is the external magnetic field along \hat{z} -direction, i_s is the z -polarized spin current injected into the magnet, and I_{s0} is the critical spin current for magnetization switching [18, 21] for a magnet with PMA, given by

$$I_{s0} = \frac{4q}{\hbar} \Delta_B \alpha_g, \quad (\text{D2})$$

where $\hbar = h/(2\pi)$ and α_g is the Gilbert damping constant.

We consider the case with no external field i.e. $H_{ext} = 0$ which from Eqs. (D1) and (D2) gives

$$\rho(m_z) = \frac{1}{Z} \exp\left(\frac{\Delta_B}{k_B T} m_z^2 + \left(\frac{i_s}{\frac{2q}{\hbar} k_B T \alpha_g}\right) m_z\right). \quad (\text{D3})$$

We consider very low energy barrier magnet i.e. $\frac{\Delta_B}{k_B T} \rightarrow 0$, which in Eq. (D3) yields

$$\rho(m_z) = \frac{1}{Z} \exp\left(\frac{i_s}{\frac{2q}{\hbar} k_B T \alpha_g} m_z\right). \quad (\text{D4})$$

The long time averaged magnetization $\langle m_z \rangle$ is defined as

$$\langle m_z \rangle = \frac{\int_{\phi=-\pi}^{\phi=\pi} \int_{\theta=0}^{\theta=\pi} m_z \rho(m_z) d\theta d\phi}{\int_{\phi=-\pi}^{\phi=\pi} \int_{\theta=0}^{\theta=\pi} \rho(m_z) d\theta d\phi}, \quad (\text{D5})$$

with $(m_z, m_x, m_y) \equiv (\cos \theta, \sin \theta \cos \phi, \sin \theta \sin \phi)$. Combining Eq. (D5) with Eq. (D4) we get the long time averaged magnetization $\langle m_z \rangle$ for a very low barrier PMA without external magnetic field as

$$\langle m_z \rangle = \coth \left(\frac{i_s}{\frac{2q}{\hbar} k_B T \alpha_g} \right) - \frac{\frac{2q}{\hbar} k_B T \alpha_g}{i_s}, \quad (\text{D6})$$

which is a Langevin function $L(x)$ of $x \equiv i_s / (\frac{2q}{\hbar} k_B T \alpha_g)$.

Note that Eq. (D6) was derived assuming $\frac{\Delta_B}{k_B T} \rightarrow 0$, however, the expression remains reasonably valid up to $\Delta_B \approx k_B T$. We have compared Eq. (D6) with numerical calculations directly from Eqs. (D3) and (D5) for $\Delta_B = 0.1k_B T$ and $k_B T$ respectively, which shows reasonably good agreement (see Fig. 5). $\Delta_B > k_B T$ the simple expression in Eq. (D6) deviates from Eqs. (D3) and (D5).

For an estimation of the pinning spin current we can approximate the Langevin function $L(x) \approx \tanh \frac{x}{3}$, hence

$$\langle m_z \rangle \approx \tanh \left(\frac{i_s}{\frac{6q}{\hbar} k_B T \alpha_g} \right). \quad (\text{D7})$$

Note that i_s from SML materials are related to input charge current i_c with a conversion factor β given by

$$i_s = \beta i_c. \quad (\text{D8})$$

Combining Eq. (D8) with Eq. (D7) yields

$$\langle m_z \rangle \approx \tanh \left(\frac{i_c}{\frac{6q k_B T \alpha_g}{\hbar \beta}} \right). \quad (\text{D9})$$

Comparing Eq. (D9) with Eq. (2) in the main manuscript yields

$$I_0 \approx \frac{6q k_B T \alpha_g}{\hbar \beta},$$

which gives the Eq. (5) in the main manuscript.

Appendix E: Angular Momentum Conservation

This section discusses the cut-off frequency of the proposed device using detailed SPICE simulations.

The proposed rectifier in Fig. 1(a) of the main manuscript converts the input ac current into a dc voltage. The dc voltage as a function of input ac current frequency is shown in Fig. 6(a) (similar to Fig. 3(a) in the main manuscript), which shows that there is a cut-off

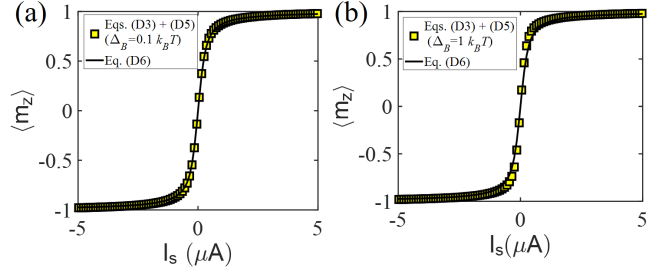


FIG. 5. Comparison of simple expression in Eq. (D6) which assumes $\Delta_B \rightarrow 0$ with the numerical calculation from Eqs. (D3) and (D5) for (a) $\Delta_B = 0.1k_B T$ and (b) $\Delta_B = 1k_B T$. This comparison indicates that Eq. (D6) is reasonably valid for $0 \leq \Delta_B \leq 1k_B T$.

frequency for the rectification. An empirical expression for the cut-off frequency, obtained from the detailed s-LLG simulations in SPICE is given in Eq. (8) of the main manuscript. In order to extract an expression we defined the cut-off frequency such that the rectified dc voltage is decreased by an order of magnitude compared to the low frequency region where dc voltage vs. frequency is flat.

The cut-off frequency f_c is related to the angular momentum conservation within the magnet. If the frequency f of input current i_c is slow such that the transferred spins from SML channel to the LBM satisfies the angular momentum conservation, then the magnetization of the LBM will follow the input current at the same frequency. We have evaluated this using detailed time-dependent SPICE simulation using the SPICE setup in Fig. 4. Figs. 6(b) and (c) shows the time-dependent response for input current with two different frequencies: (#1) below the cut-off (see Fig. 6(b)) and (#2) above the cut-off (see Fig. 6(c)). The magnetization m_z of the LBM smoothly follows the input ac current i_c with frequency below cut-off frequency which leads to a rectified dc voltage between LBM and the reference and charges up the capacitor C_0 .

However, when the input ac current i_c has a frequency above the cut-off f_c , m_z struggles to follow i_c (see Fig. 6(c)) since frequency is fast enough that the spin transferred from the SML channel to the LBM do not satisfy the angular momentum conservation principle. There is no net rectification since m_z do not follow i_c and we do not observe any dc voltage across the capacitor. The observation in Fig. 6 is valid for LBM with both PMA and IMA.

Appendix F: Power Conversion Efficiency

This section discusses the ac to dc power conversion efficiency and provides the details of derivation of Eq. (7) in the main manuscript.

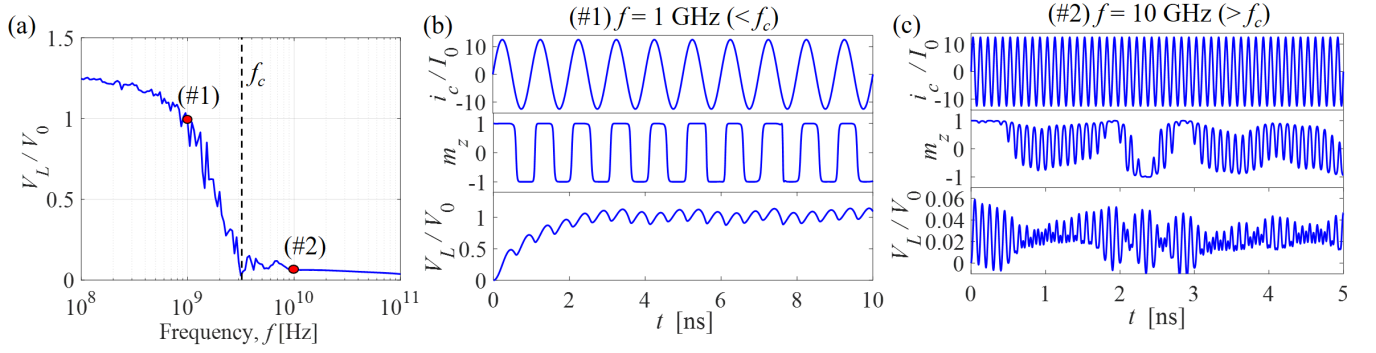


FIG. 6. SPICE simulation of a low barrier magnet (LBM) and result applies to both IMA and PMA. (a) Open circuit dc voltage of the rectifier vs. input ac frequency. We observe time-dependent characteristics of the device at two frequency points: (b) below cut-off (1) and (c) above cut-off (2). The magnetization m_z follows the input ac current i_c below cut-off frequency smoothly resulting in rectification and charging up a capacitor. However, m_z struggles to follow the input ac current i_c above the cut-off frequency and there is no dc voltage to charge up the capacitor.

Under the no load condition ($R_L \rightarrow \infty$), we have the open circuit dc voltage $V_L|_{R_L \rightarrow \infty} = \langle V_{fm} \rangle$. From Eq. (C4) we know that for $i_{c0} \ll I_0$

$$\langle V_{fm} \rangle = \frac{\alpha \xi p_0 p f}{2 G_B R_{ch} I_0} P_{in},$$

and from Eq. (C2) we know that for $i_{c0} \gg I_0$

$$\langle V_{fm} \rangle = \frac{\alpha \xi p_0 p f}{\pi G_B} \times \frac{\sqrt{2}}{\sqrt{R_{ch}}} \times \sqrt{P_{in}}.$$

Under the short circuit condition ($R_L \rightarrow 0$), we have the short circuit dc current $I_L|_{R_L \rightarrow 0} = \langle V_{fm} \rangle / R_{eq}$, where R_{eq} is the equivalent resistance between the LBM and the reference NM.

The maximum power transferred to the load is given by

$$P_{L,\max} = \frac{1}{4} \times V_L|_{R_L \rightarrow \infty} \times I_L|_{R_L \rightarrow 0} = \frac{\langle V_{fm} \rangle^2}{4 R_{eq}}. \quad (\text{F1})$$

which yields

$$\begin{aligned} P_{L,\max} &= \left(\frac{\alpha \xi p_0 p f}{2 G_B R_{ch} I_0} \right)^2 \frac{P_{in}^2}{4 R_{eq}} \quad \text{for } i_{c0} \ll I_0 \\ &= \left(\frac{\alpha \xi p_0 p f}{\pi G_B} \right)^2 \frac{P_{in}}{2 R_{ch} R_{eq}} \quad \text{for } i_{c0} \gg I_0. \end{aligned} \quad (\text{F2})$$

The ac to dc power conversion efficiency is given by

$$\begin{aligned} \eta &= \frac{dP_{L,\max}}{dP_{in}} = \left(\frac{\alpha \xi p_0 p f}{2 G_B R_{ch} I_0} \right)^2 \frac{P_{in}}{2 R_{eq}} \quad \text{for } i_{c0} \ll I_0 \\ &= \left(\frac{\alpha \xi p_0 p f}{\pi G_B} \right)^2 \frac{1}{2 R_{ch} R_{eq}} \quad \text{for } i_{c0} \gg I_0. \end{aligned} \quad (\text{F3})$$

Note that η increases with input ac power P_{in} and reaches a maximum when $i_{c0} \gg I_0$ given by

$$\eta_{\max} = \left(\frac{\alpha \xi p_0 p f}{\pi G_B} \right)^2 \frac{1}{2 R_{ch} R_{eq}}. \quad (\text{F4})$$

-
- [1] E. E. Fullerton and J. R. Childress, Proceedings of the IEEE **104**, 1787 (2016).
 - [2] G. Prenat, K. Jabeur, G. D. Pendina, O. Boule, and G. Gaudin, “Beyond stt-mram, spin orbit torque ram sot-mram for high speed and high reliability applications, spintronics-based computing,” (Springer International Publishing, Switzerland, 2015) pp. 145–157, doi: 10.1007/978-3-319-15180-9_4.
 - [3] B. Parks, M. Bapna, J. Igbokwe, H. Almasi, W. Wang, and S. A. Majetich, AIP Advances **8**, 055903 (2018), <https://doi.org/10.1063/1.5006422>.
 - [4] D. Vodenicarevic, N. Locatelli, A. Mizrahi, J. S. Friedman, A. F. Vincent, M. Romera, A. Fukushima, K. Yakushiji, H. Kubota, S. Yuasa, S. Tiwari, J. Grollier, and D. Querlioz, Phys. Rev. Applied **8**, 054045 (2017).
 - [5] N. Locatelli, A. Mizrahi, A. Accioly, R. Matsumoto, A. Fukushima, H. Kubota, S. Yuasa, V. Cros, L. G. Pereira, D. Querlioz, J.-V. Kim, and J. Grollier, Phys. Rev. Applied **2**, 034009 (2014).
 - [6] K. Y. Camsari, R. Faria, B. M. Sutton, and S. Datta, Phys. Rev. X **7**, 031014 (2017).
 - [7] A. Mizrahi, T. Hirtzlin, A. Fukushima, H. Kubota, S. Yuasa, J. Grollier, and D. Querlioz, Nature Commun. **9**, 1533 (2018).
 - [8] C. H. Li, O. M. J. van t Erve, J. T. Robinson, Y. Liu, L. Li, and B. T. Jonker, Nat. Nanotechnol. **9**, 218 (2014), doi: 10.1038/nnano.2014.16.
 - [9] L. Liu, A. Richardella, I. Garate, Y. Zhu, N. Samarth, and C.-T. Chen, Phys. Rev. B **91**, 235437 (2015).
 - [10] A. Dankert, J. Geurs, M. V. Kamalakar, S. Charpentier, and S. P. Dash, Nano Lett. **15**, 7976 (2015), doi: 10.1021/acs.nanolett.5b03080.
 - [11] V. T. Pham, L. Vila, G. Zahnd, A. Marty, W. Saverio-Torres, M. Jamet, and J.-P. Attan, Nano Lett. **16**, 6755 (2016).
 - [12] J.-H. Lee, H.-J. Kim, J. Chang, S. H. Han, H.-C. Koo, S. Sayed, S. Hong, and S. Datta, Scientific Reports (Accepted) (2018).
 - [13] S. Sayed, S. Hong, and S. Datta, arXiv:1707.04051 [cond-mat.mes-hall] (2017).

- [14] P. Debashis, R. Faria, K. Y. Camsari, J. Appenzeller, S. Datta, and Z. Chen, in *2016 IEEE International Electron Devices Meeting (IEDM)* (2016) pp. 34.3.1–34.3.4.
- [15] K. Y. Camsari, S. Ganguly, and S. Datta, *Sci. Rep.* **5**, 10571 (2015).
- [16] S. Hong, V. Diep, S. Datta, and Y. P. Chen, *Phys. Rev. B* **86**, 085131 (2012).
- [17] S. Sayed, S. Hong, and S. Datta, *Sci. Rep.* **6**, 35658 (2016).
- [18] S. Sayed, S. Hong, E. E. Marinero, and S. Datta, *IEEE Electron Device Letters* **38**, 1665 (2017).
- [19] J. Kim, C. Jang, X. Wang, J. Paglione, S. Hong, and D. Kim, arXiv:1809.04977 [cond-mat.str-el] (2018).
- [20] P. Li, W. Wu, Y. Wen, C. Zhang, J. Zhang, S. Zhang, Z. Yu, S. A. Yang, A. Manchon, and X.-x. Zhang, *Nature Communications* **9**, 3990 (2018).
- [21] J. Z. Sun, *Phys. Rev. B* **62**, 570 (2000), doi: 10.1103/PhysRevB.62.570.
- [22] P. Debashis, R. Faria, K. Y. Camsari, and Z. Chen, *IEEE Magnetics Letters* **9**, 1 (2018).
- [23] K. Y. Camsari, S. Ganguly, S. Sayed, and S. Datta, “Modular approach to spintronics,” (2013), <https://nanohub.org/groups/spintronics>.
- [24] Y. G. Semenov, X. Duan, X.-L. Li, and K. W. Kim, *Journal of Physics and Chemistry of Solids* (2017), <https://doi.org/10.1016/j.jpics.2017.07.020>.
- [25] P. Jacquod, R. S. Whitney, J. Meair, and M. Büttiker, *Phys. Rev. B* **86**, 155118 (2012).
- [26] A. A. Tulapurkar, Y. Suzuki, A. Fukushima, H. Kubota, H. Maehara, K. Tsunekawa, D. D. Djayaprawira, N. Watanabe, and S. Yuasa, *Nature* **438**, 339 (2005).
- [27] S. Miwa, S. Ishibashi, H. Tomita, T. Nozaki, E. Tamura, K. Ando, N. Mizuochi, T. Saruya, H. Kubota, K. Yakushiji, T. Taniguchi, H. Imamura, A. Fukushima, S. Yuasa, and Y. Suzuki, *Nature Materials* **13**, 50 (2013), article.
- [28] B. Fang, M. Carpentieri, X. Hao, H. Jiang, J. A. Katine, I. N. Krivorotov, B. Ocker, J. Langer, K. L. Wang, B. Zhang, B. Azzerboni, P. K. Amiri, G. Finocchio, and Z. Zeng, *Nature Communications* **7**, 11259 (2016), article.
- [29] B. Fang, M. Carpentieri, S. Louis, V. Tiberkevich, A. Slavin, I. N. Krivorotov, R. Tomasello, A. Giordano, H. Jiang, J. Cai, Y. Fan, Z. Zhang, B. Zhang, J. A. Katine, K. L. Wang, P. K. Amiri, G. Finocchio, and Z. Zeng, arXiv:1801.00445 [physics.app-ph] (2018).
- [30] W. H. Butler, T. Mewes, C. K. A. Mewes, P. B. Visscher, W. H. Rippard, S. E. Russek, and R. Heindl, *IEEE Transactions on Magnetics* **48**, 4684 (2012).
- [31] L. Liu, O. J. Lee, T. J. Gudmundsen, D. C. Ralph, and R. A. Buhrman, *Phys. Rev. Lett.* **109**, 096602 (2012), doi: 10.1103/PhysRevLett.109.096602.
- [32] W. J. Wang, K. H. Gao, and Z. Q. Li, *Scientific Reports* **6**, 25291 EP (2016), article.
- [33] G. Fischer, H. Hoffmann, and J. Vancea, *Phys. Rev. B* **22**, 6065 (1980), doi: 10.1103/PhysRevB.22.6065.
- [34] B. Behin-Aein, A. Sarkar, S. Srinivasan, and S. Datta, *Appl. Phys. Lett.* **98**, 123510 (2011), <https://doi.org/10.1063/1.3567772>.
- [35] C. Dagdeviren, Z. Li, and Z. L. Wang, *Annual Review of Biomedical Engineering* **19**, 85 (2017), PMID: 28633564, <https://doi.org/10.1146/annurev-bioeng-071516-044517>.